remote sensing

MDPI

Article

Interferometric Synthetic Aperture Radar Phase Linking with Level 2 Coregistered Single Look Complexes: Enhancing Infrastructure Monitoring Accuracy at Algeciras Port

Jaime Sánchez-Fernández [1,2,3], Alfredo Fernández-Landa [2,3,*], Álvaro Hernández Cabezudo [2,3] and Rafael Molina Sánchez [4]

[1] ETSI Navales, Universidad Politécnica de Madrid (UPM), Av. Universidad Politécnica de Madrid, 28040 Madrid, Spain; jaime.sanchezfer@alumnos.upm.es
[2] Department of Land Morphology & Engineering, ETSI Caminos, Canales y Puertos, Universidad Politécnica de Madrid (UPM), 28040 Madrid, Spain; ahernandez@detektia.com
[3] Detektia Earth Surface Monitoring S.L., C/ Faraday 7, 28049 Madrid, Spain
[4] CEHINAV, DITTU, ETSI de Caminos, Canales y Puertos, Universidad Politécnica de Madrid (UPM), 28040 Madrid, Spain; rafael.molina@upm.es
* Correspondence: afernandez@detektia.com; Tel.: +34-644-081-332

Abstract: This paper presents an advanced workflow for processing radar imagery stacks using Persistent Scatterer and Distributed Scatterer Interferometry (PSDS) to enhance spatial coherence and improve displacement detection accuracy. The workflow leverages Level 2 Coregistered Single Look Complex (L2-CSLC) images generated by the open-source COMPASS (Coregistered Multi-temporal Sar SLC) framework in combination with the Combined eigenvalue maximum likelihood Phase Linking (CPL) approach implemented in MiaplPy. Starting the analysis directly from Level 2 products offers a significant advantage to end-users, as they simplify processing by being pre-geocoded and ready for immediate analysis. Additionally, the open-source nature of the workflow and the use of L2-CSLC products simplify the processing pipeline, making it easier to distribute directly to users for practical applications in monitoring infrastructure stability in dynamic environments. The ISCE3-MiaplPy workflow is compared against ISCE2-MiaplPy and the European Ground Motion Service (EGMS) to assess its performance in detecting infrastructure deformations in dynamic environments, such as the Algeciras port. The results indicate that ISCE3-MiaplPy delivers denser measurements, albeit with increased noise, compared to its counterparts. This higher resolution enables a more detailed understanding of infrastructure stability and surface dynamics, which is critical for environments with ongoing human activity or natural forces.

Keywords: phase linking; coregistered SLCs; Algeciras Port; geometric accuracy; ETAD corrections; Sentinel-1; radar imaging

check for updates

Citation: Sánchez-Fernández, J.; Fernández-Landa, A.; Hernández Cabezudo, Á.; Molina Sánchez, R. Interferometric Synthetic Aperture Radar Phase Linking with Level 2 Coregistered Single Look Complexes: Enhancing Infrastructure Monitoring Accuracy at Algeciras Port. *Remote Sens.* **2024**, *16*, 3966. https://doi.org/10.3390/rs16213966

Academic Editor: Michele Saroli

Received: 20 September 2024
Revised: 22 October 2024
Accepted: 23 October 2024
Published: 25 October 2024

Copyright: © 2024 by the authors. Licensee MDPI, Basel, Switzerland. This article is an open access article distributed under the terms and conditions of the Creative Commons Attribution (CC BY) license (https://creativecommons.org/licenses/by/4.0/).

1. Introduction

The sustainability and resilience of port infrastructure are essential for the global economy, as they directly impact trade, economic growth, and environmental conservation [1]. Implementing a timely and efficient maintenance strategy is crucial to monitor the regular operation of port infrastructures, especially as harsh environmental conditions in ports can deteriorate their structural functionality [2].

The monitoring and control of damage to port infrastructure lies in the need to develop advanced management strategies that require a deep understanding of the spatial and temporal evolution of damage during the useful life of the structures. In particular, high spatial and temporal resolution monitoring of the geometrical evolution of port infrastructure is a fundamental input in damage assessment. The geometrical evolution of a breakwater, its overtopping protection walls, or the sliding or tilting of a caisson is not a failure of a structure per se. The combination of three-dimensional behavior with climatic, geotechnical,

or operational boundary conditions, or the existence of extraordinary actions on elements or sections of work, allows for the prevention and prediction of mitigating and corrective actions aimed at maximizing safety and minimizing construction and operating costs. In this context, the definition of the concept of damage in port infrastructure, its evolution, and the methodologies used to evaluate its progression are of significant importance [3,4].

By monitoring and controlling damage, it becomes possible to assess structural stability and make informed decisions about maintenance, repair, and potential upgrades, thus contributing to the sustainability and resilience of the port infrastructure. Currently, port infrastructure monitoring relies on conventional topographic and geotechnical approaches. Common techniques for tracking subsidence and minor changes in engineering structures include precision surveying (leveling), inclinometers, UAV photogrammetry, laser scanning, and global navigation satellite systems [5]. Although contact methods utilizing accelerometers and fiber optics can rapidly monitor crucial construction points, they prove impractical for overseeing the entire infrastructure due to their time-consuming and budget-intensive nature.

These control and monitoring systems typically incur significant costs, which require field instrumentation. Moreover, measurements are often either non-existent or not conducted at the required frequency. Topographic and geotechnical campaigns, when available, lack uniformity in terms of techniques, data resolution, and temporal continuity, thus complicating their analysis. The inherent complexity, lack of standardization, and frequent absence of digitization and data integration make it difficult to anticipate the long-term behavior of various components within port infrastructure, hindering the development of an effective early warning system.

Despite the existence of measurements to assess deformation and structural conditions, there is a notable scarcity of developed early warning systems. This scarcity poses a challenge in facilitating timely decision-making on when and to what extent interventions are necessary to prevent irreversible damage to port infrastructure. Satellite-based Interferometric Synthetic Aperture Radar (InSAR) technology could solve many of the problems and limitations of more traditional techniques, as (i) it does not require instrumentation or on-site personnel, (ii) it provides homogeneous and comparable historical ground motion information throughout the port, (iii) it generates a high density of deformation monitoring points, (iv) it can cover large areas in a cost-effective way [6], and (v) it allows for constant updates and fine-tuning of warning systems.

InSAR has emerged as a critical tool for monitoring and analyzing dynamic landscapes, particularly in areas of intense human activity such as ports [7,8]. In particular, methodologies that exploit persistent and distributed scatterers (PSDS) such as MiaPLpy software (MIAmi Phase Linking software in PYthon v0.2.1) [9] using a coregistered stack processed with InSAR Scientific Computing Environment 2 (ISCE2) [10] have been successfully applied to the monitoring of ports [11], subsidence [12], and reservoirs [13].

As one of the busiest maritime hubs, the Port of Algeciras represents an ideal case study for testing and refining InSAR-based monitoring systems. Accurate and reliable spatial data are critical in this dynamic environment, where informed decisions can significantly impact operational efficiency and structural resilience.

In this study, we evaluated a new open-source workflow for generating InSAR deformation point clouds in port environments, combining Sentinel-1 Coregistered Single Look Complex (CSLC) data with MiaPLpy software. The CSLC products are generated using the COMPASS workflow [14–16] from the OPERA JPL team, which computes the timing corrections and then is geocoded using ISCE3 [17]. Unlike the previous ISCE2-based method based on Enhanced Spectral Decomposition [10], COMPASS integrates a more advanced coregistration approach, MAGIC, that adjusts for residual misregistrations using external models and corrections [18,19].

To validate this workflow, we compare its results with previous ISCE2-MiaPLpy implementations and the European Ground Motion Service (EGMS) time series for the

port of Algeciras. Specifically, we assess three key metrics: area coverage, noise in the time series, and the distribution of ground deformation velocities.

Area of Study

The study area is located in the Port of Algeciras in the Bay of Algeciras in Southern Spain (Figure 1). This port is a crucial maritime hub in Europe and a significant gateway to the Mediterranean Sea.

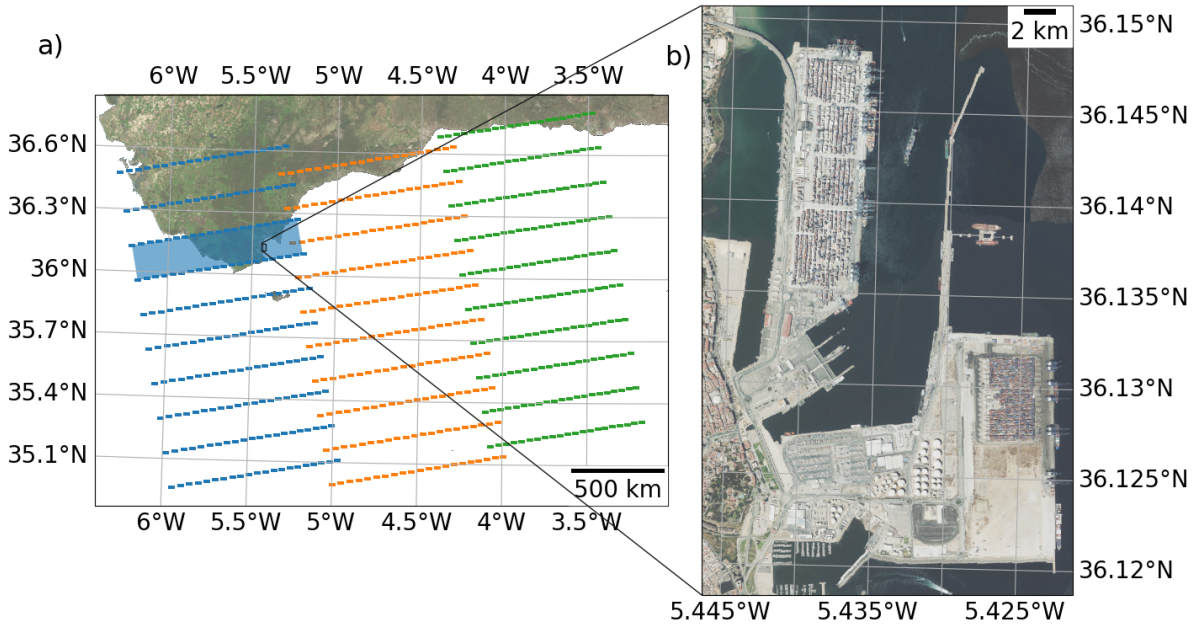


Figure 1. (**a**) Three swaths from the interferometric wide swath mode ascending Track 74. Algeciras port is located in the IW1 and burst t074-157011-iw1 (Blue rectangle) was processed (**b**) AOI processed with PSDS software.

The Port of Algeciras Bay is a key player in the Western Mediterranean, with a scale-free maritime network [20]. It serves as a gateway city connecting Europe and Africa and has experienced significant transformations in recent years [21]. The port's competitiveness in container traffic is influenced by factors such as transshipment and maritime accessibility [22]. In terms of efficiency, it ranks among the top Spanish ports, particularly in transshipment activities [23].

2. Materials and Methods

2.1. Data Used

2.1.1. EGMS

The results obtained in this work were compared with the European Ground Motion Service (EGMS) level 2a product [24] using the 2018–2022 update [25]. EGMS provides homogeneous information on ground movements in Europe on a continental scale and is updated annually. EGMS processes the same source of SAR information used in this work from Sentinel-1A and Sentinel-1B twin satellites of the Copernicus Program from the European Union.

EGMS products are made by a consortium comprising four different InSAR Processing Entities (IPE). Consequently, there are differences in the processing algorithms implemented in the different processing chains. Although all are based on advanced PS and DS InSAR processing techniques, the end products have the same attributes, and all meet the project requirements in terms of quality, consistency, and homogeneity. Overlaps between adjacent processing areas are also used to check and ensure seamless harmonization between adjacent Sentinel-1 tracks and the different processing chains.

2.1.2. Sentinel-1A and B Dataset

A total of 270 SAR images were processed (Table 1), including both ascending and descending geometries from Sentinel-1 constellation satellites A and B. All images are single-look complex (SLC) TOPSAR data acquired in Interferometric Wide (IW) swath mode with VV polarization for the time frame of 10 January 2020 to 27 December 2022, coinciding with the temporal extent of the EGMS 2023 update.

Table 1. Sentinel-1 images used.

Satellite	Ndates	First Date	Last Date	Geometry	Track
Sentinel-1A	150	10 January 2018	27 December 2022	Ascending	74
Sentinel-1B	120	4 January 2018	14 December 2021	Ascending	74

Precise orbit files produced within 20 days of the sensing time with an accuracy margin of 5 cm in 3D RMS are employed for image processing.

2.1.3. Copernicus DEM

The Copernicus Digital Elevation Model (DEM) Cop-GLO30 [26] is used throughout the InSAR processing chain in this work. This is the same DEM used by EGMS. The Copernicus DEM is derived from the WorldDEM, an edited Digital Surface Model that features flattened water bodies, consistent river flows, and edited shorelines, coastlines, airports, and terrain structures. The WorldDEM product is based on radar satellite data from the TanDEM-X mission.

2.1.4. ETAD Dataset

We used state-of-the-art corrections for the most important sources of error in TOPS interferometry and obtained the precise geolocalization (CSLC experiments accuracy) using Sentinel-1 Extended Timing Annotation Processor (SETAP) [27,28].

2.1.5. Tropospheric and Ionospheric Information

For the estimation and subtraction of the tropospheric delay, we used RAiDER [29]. The weather model date used for the troposphere layer was ERA5 [30], while the IONEX NASA product [31] was used for the ionosphere Total Electron Content (TEC).

2.2. Methods

The proposed method (Figure 2) involves generating a stack of Coregistered Single-Look Complex (CSLC) data using the COMPASS (Version 0.5.5)workflow developed by the OPERA project and ISCE3 software (Version 0.22.1). Although Level 2 CSLC products for all of North America are available for download via the Alaska Satellite Facility (ASF), we processed the Level 1 Single Look Complex (L1-SLC) images to generate Level 2 (L2) CSLC data specific to our study area—the Port of Algeciras.

Level 0 (L0) products consist of compressed and unfocused raw data. The Level 1 (L1) products are focused georeferenced data using orbit and attitude information from the satellite, provided in slant-range geometry. In contrast to Level 2 (L2), as the coregistered single look complex (L2-CSLC) [14], products derived from the L1 single look complex (SLC) product are outputted in the projected map system, making it ready for analysis.

In the phase linking step, the coherence matrix of each image pixel is estimated, representing all possible interferograms over a set of N images for that pixel. For each pixel, the absolute values of the coherence matrix represent the interferometric correlation, ranging between 0 and 1. The phase of the off-diagonal elements corresponds to the averaged phase of each interferogram for that specific pixel. The coherence matrix of a PS shows all correlation values equal to 1, as it is not multilooked. An optimum set of N phase values is then extracted from each matrix. Following the Maximum Likelihood Estimation (MLE) of the optimum phase values, the process continues as with standard PSI algorithms.

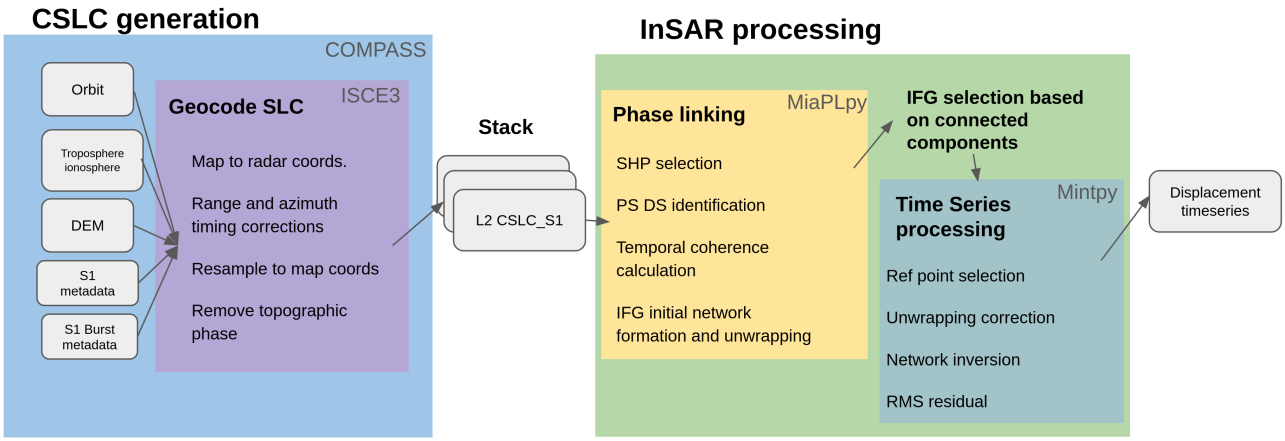


Figure 2. Proposed workflow schema.

We used MiaPlPy and MintPy with minor modifications to work with CSLCs. SqueeSAR [32] is another example of such algorithms that exploits both Persistent Scatterer (PS) and Distributed Scatterer (DS) information over a stack segment using phase linking (PL) to obtain displacement time series. For validation purposes, we compared the ISCE3-MiaPlPy workflow with two other approaches:

- ISCE2-MiaPlPy Workflow: Uses ISCE2's TopStack processor (Version 2.4.2) [10] to generate the coregistered stack. The main difference with the ISCE3 approach is that TopStack uses enhanced spectral diversity to meet the required azimuth misregistration errors, while COMPASS implements a model-adjusted geometrical image coregistration (MAGIC) [18,19] that estimates the residual misregistration using external models and products, e.g., ionosphere, troposphere, solid Earth tides, plate motion, and SAR processing effects. The rest of the process is otherwise identical, using MiaPlPy and MintPy to obtain the displacement time series.
- European Ground Motion Service (EGMS): Provides preprocessed ground motion data derived from Sentinel-1 SAR imagery. It uses a semi-standardized processing chain throughout Europe with slight modifications between different providers [33].

2.2.1. Coregistered CSLC Stack

Regular Sentinel-1 SLC products are provided in a range-Doppler coordinate system. The grid is not aligned over multiple acquisitions, so a coregistration process is normally used to align all images to the reference system of the master. The CSLC coregistration output is provided in the chosen Coordinate Reference System (CRS). All images are resampled to a common grid of 10 m × 5 m in Northing and Easting coordinates [34], and S1 Instrument Processing Facility (IPF) artifacts (i.e., bistatic delay, geometry steering Doppler, and azimuth FM rate mismatch) [27], atmospheric effects (i.e., ionosphere and static troposphere), and the Solid Earth tide effects [19] are estimated and removed.

The geocoded SLC phase is adjusted using a reference orbit and a DEM to eliminate the topographic phase components [35]. The CSLC product's sampling interval along the map's coordinate directions is comparable to that of the original full-resolution SLC product. Nonetheless, before resampling and interpolation of the data, the linear slope introduced by the electronic steering of the antenna needs to be corrected [36].

Since the CSLC phase is flattened, the phase difference between two CSLC products acquired on the same relative orbit produces an interferogram referring only to surface displacement and noise (i.e., no topographic fringes). This product specification includes definitions for auxiliary static datasets that contain rasterized data on Line of Sight (LOS), incidence angle, coordinates, layover, and shadow masks for each point, along with processing quality assurance information. The CSLC product can be opened using any geo-

graphical information software (GIS) or integrated with other geographic data products to generate interferograms and other applications.

Timing Corrections

ETAD gridded corrections for S-1 are applied to the SLC data for each burst, with the positions of the original pixels defined by the annotated time coordinates (t, τ). Initially, the time-annotated ETAD correction grids must be resampled to the SLC resolution using a simple bilinear interpolation. The combined ETAD range corrections, $\Delta_\tau(t, \tau)$, and azimuth corrections, $\Delta_t(t, \tau)$, are then subtracted from the original SLC slant range and azimuth timings, resulting in an irregularly gridded but timing-corrected SLC dataset. The different timing corrections applied are as follows:

- Range shift due to Doppler: Due to the fact that a single transmitted radar pulse is reflected by different targets with different sensor-to-target geometries, several Doppler shifts are superimposed within one received range line. Therefore, a compensation of the Doppler effect immediately after receiving is not possible. This is translated as a range shift in TOPS interferometry [37]:

$$\Delta\tau_{Doppler} = -\Delta f_{Doppler}(t)/K_r \quad (1)$$

  where $\Delta f_{Doppler}$ is the total Doppler (geometric Doppler + steering Doppler), and K_r is the FM-rate of the range chirp [37–40]
- Bistatic Azimuth Effects Mitigation: The IPF applies the stop-and-go approximation in the processing of the S-1 acquisitions that assumes that the satellite is in the same position for the emission and reception. In reality, the motion of the platform between pulses amounts to tens of meters that produces a shift in azimuth. To correct for this effect, we must reverse the original shift and apply the precise one:

$$\Delta t_{BA} = \tau_{mid}/2 - \tau_g/2 - rank \cdot PRI \quad (2)$$

  Here, τ_{mid} denotes the reconstructed mid-swath range time, τ_g stands for the range time at the correction grid point, and PRI corresponds to the pulse repetition interval for the burst in question. The parameter *rank* indicates the number of PRI events between the transmission of the pulse and the reception of its echo.
- Azimuth FM mismatch mitigation: This is a topography-correlated error that stems from a constant effective velocity parameter used in the azimuth FM rate calculation during the processing of extensive azimuth blocks. For stripmap SAR with zero-Doppler steering, the mismatch effect (quadratic phase error) primarily causes image defocusing. However, for TOPS products, it also results in azimuth shifts.
- Solid Earth tides refer to the distortions in the Earth's crust due to the gravitational influences of the Sun and the Moon. These deformations usually fluctuate by ±25 cm vertically, and there is also notable horizontal movement reaching up to 6 cm. For the calculation, we use Python-based solid Earth tides (PySolid) [19,41].
- Ionosphere delay in line-of-sight direction calculated from the TEC obtained from IONEX NASA product [31].
- Wet and dry LOS tropospheric delay: containing the LOS wet and dry troposphere delays computed from the respective dry and wet pressure obtained from the ERA5 model [30] preprocessed with RAiDER [29].

2.2.2. Phase Linking

Following coregistration, the geocoded stack of radar images undergoes phase linking [42–44], a crucial process for consolidating spatial information from distributed reflectors across multiple acquisitions. Phase linking involves the coherent combination of radar images, which enhances the overall clarity and resolution of the composite image by minimizing phase inconsistencies and reducing artifacts such as speckle noise. Additionally, the virtual images generated through phase linking assist in recovering long-term coherence

for distributed scatterers [9,45,46]. This is achieved by stacking multiple acquisitions and applying multi-looking techniques, which enhance the signal-to-noise ratio and ensure sustained coherence over extended periods [42].

The enhanced composite image produced through phase linking serves as a robust foundation for the following notable applications:

- Subsidence analysis: Improved phase coherence and reduced artifacts enable more accurate detection and monitoring of ground deformation over time, facilitating reliable subsidence measurements.
- Coherence analysis: Enhanced image clarity allows for a precise assessment of temporal coherence, which aids in the identification of areas with significant changes or persistent stability.

By recovering long-term coherence, phase linking supports more reliable monitoring and analysis of distributed scatterer behavior within the Algeciras Port, thereby enhancing the accuracy and reliability of subsidence and coherence analyses.

The first approach developed to estimate the deterministic component of the observer phases in coregistered InSAR stacks was persistent scatterer interferometry (PSI), which relies on bright scatterers smaller than the resolution cell with a good signal-to-noise ratio (SNR). Another family of algorithms uses distributed scatterers, which are usually multiple smaller scatterers that share statistical characteristics over an extended area and experience decorrelation during the time series. The first algorithm to use this was the Small Baseline Subset (SBAS) technique [47], which uses reduced spatial resolution and limits itself to the most coherent interferograms to overcome decorrelation effects. The other approach used is PL, which employs all the possible interferograms given a set of observation dates. This enhances the SNR and consequently also improves the displacement detection accuracy.

For a pixel at location x in a CSLC stack, a complex N × 1 target vector d is given as follows:

$$d_x(A,\theta) = \left[A_1 e^{i\theta_x^1}, A_2 e^{i\theta_x^2}, \ldots, A_N e^{i\theta_x^N},\right] \tag{3}$$

To take full advantage of the interferometric information, we estimate the N × N covariance matrix for a pixel P. We first need to find a neighborhood with Statistical Homogeneous Pixels (SHP) [32]. In order to find these groups of pixels, we evaluate the homogeneous similarity of the surroundings using a Kolmogorov–Smirnov test in a 15 × 15 square patch around each pixel. Once we have the SHPs, the complex covariance matrix (CCM) is defined as follows [48]:

$$\hat{C}_{ij} = \frac{1}{N_{SHP_p}} \sum_{x \in SHP_p} d_x^i {d_x^j}^* \tag{4}$$

where * denotes the complex conjugation operation and N_{SHP} is the total number of SHP groups. The coherence matrix is defined as the magnitude of the CCM normalized by the amplitude:

$$\left|\hat{\Gamma}_{ij}\right| = \left|\hat{C}_{ij}\right| / \sqrt{\sum_{x \in SHP_p} d_x^i {d_x^i}^* \sum_{x \in SHP_p} d_x^j {d_x^j}^*} \tag{5}$$

This matrix is the maximum likelihood estimation of the second order moment for the SAR data over a neighborhood of pixels. Different PL methods assume different factorization model for the coherence matrix [48]. Under this assumption, computing the estimated wrapped phases corresponds to computing the eigenvector corresponding to the minimum eigenvalue of the following product:

$$(|\hat{\Gamma}|^{-1} \circ \hat{\Gamma})\hat{v} = \lambda_m \hat{v} \tag{6}$$

where ∘ denotes the Hadamard product. This method requires the $|\hat{\Gamma}|^{-1}$ to be semidefinite positive. If this is not true, even after adding regularization to the inversion, we take the largest eigenvector of the CCM. This method is referred to as Combined eigenvalue maximum likelihood Phase Linking (CPL) [9].

Under this model, the scattering characteristics of the DS region are estimated via a mechanism similar to PS. The MLE can be viewed as a temporal filter that reduces the data from n(n × 1)/2 interferograms to a phase sequence of length n.

The biggest disadvantage of this method is the increase in computational complexity involved in the computation of the full coherence matrix for each pixel. To avoid this, we use a sequential estimator [49], which only needs partial access to the stack and uses virtual images created from mini-stacks of a determined size l. These ministacks are isolated diagonal blocks from the coherence matrix $\hat{\Gamma}$ that are compressed temporally and then used to create artificial interferograms with newer ministacks and the latest acquisitions $l - 1$ in order to efficiently retrieve the long-term filtered coherent phase [42].

For a pixel to be selected as a PS, it should have less than 10 SHP, its amplitude dispersion index [50] should be less than 0.4, and the top eigenvalue contribution in the decomposition of Γ should be 70%. The CSLC phase for these pixels in the stack is referenced to the initial acquisition and saved as their wrapped phase series, with their temporal coherence assigned a value of 1. In ref. [9], this criteria allows us to improve the PS density and filter pixels where multi-target layover is present [51].

2.2.3. Phase Unwrapping and Optimization of the InSAR Network

Phase unwrapping is a critical step in InSAR analysis, as it transforms wrapped phase measurements into meaningful deformation or topographic information. In our analysis, all interferograms (IFGs) were unwrapped using the SNAPHU algorithm [52], which treats each interferogram independently. Unlike 3D phase unwrapping methods, such as the one implemented in StamPS [53], which incorporates temporal information, SNAPHU operates solely in the spatial domain. This limitation increases the risk of unwrapping errors, especially in areas with high temporal decorrelation or noise.

Faulty IFGs—resulting from decorrelation, sudden movements, multilooking, or other noise sources—can distort displacement measurements. To mitigate these potential errors, MiaPLpy leverages MintPy's unwrapping correction routines, which are based on the closure relationship between phase triplets [54]. These routines require a minimal set of connected points across all unwrapped IFGs to perform the correction reliably. However, achieving this in environments that are both small and subject to dynamic changes, where substantial temporal decorrelation may occur, poses significant challenges.

We constructed the InSAR network using the following selection criteria:

- Temporal baseline: A maximum temporal distance of 220 days between successive acquisitions to balance temporal resolution and coherence.
- Spatial baseline: A perpendicular baseline threshold of 200 m to ensure adequate spatial coverage and minimize decorrelation.

We used Delaunay triangulation to systematically arrange the IFGs, ensuring optimal spatial distribution and overlap across the study area [9]. This approach resulted in a Delaunay network with a larger temporal baseline threshold than the default 120 days used in MiaPLpy, thereby increasing the number of connections for each image in the IFG graph. The increased redundancy in the initial network ensures multiple overlapping measurements for each pixel, reducing the likelihood of creating disconnected subsets within the network. This strategy helps prevent the discarding of all IFGs related to a single image after the IFG selection process, which is crucial for the later displacement inversion.

We prioritized IFGs based on the number of disconnected pixels they introduced. IFGs that introduced fewer disconnected pixels were prioritized, while those significantly reducing network connectivity were discarded. This approach helped maintain a robust network and ensured that the selected IFGs would contribute effectively to the final displacement measurements.

2.2.4. Displacement Inversion

Following phase unwrapping and the correction of any inconsistencies through phase closure routines, we perform the final step: displacement inversion. This step is crucial for converting the unwrapped phase values into reliable deformation time series across the study area. Time series inversion is performed using a regularized least squares approach, employing an L1 norm to account for outliers and ensure robust solutions in the presence of noise and decorrelated areas [9].

The temporal coherence, derived during the phase linking process, is used as a weighting factor during the inversion [9]. This enhances the inversion accuracy by giving more significance to points with higher coherence, thereby minimizing the impact of noise in temporally unstable areas.

3. Results

3.1. Impact of Timing Corrections on Geocoded SLC Data

Figure 3 presents the timing corrections applied during the coregistration of a raw Sentinel-1 burst. These corrections address delays caused by atmospheric effects, tidal deformations from celestial bodies, and internal adjustments within the Sentinel-1 SAR-IPF system [14]. These corrected timings are crucial for ensuring accurate geolocation and subpixel-level feature analysis in repeat-pass interferometry [28]. These corrections are generated using a coarse grid and then upscaled to match the original SLC.

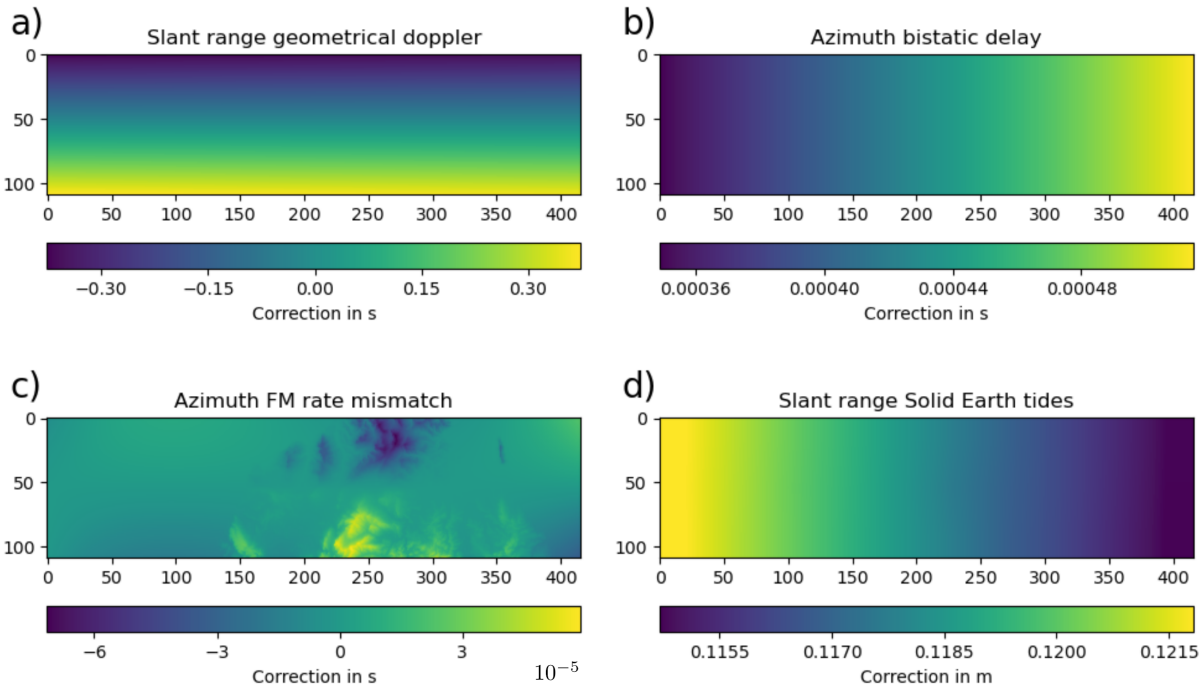


Figure 3. *Cont.*

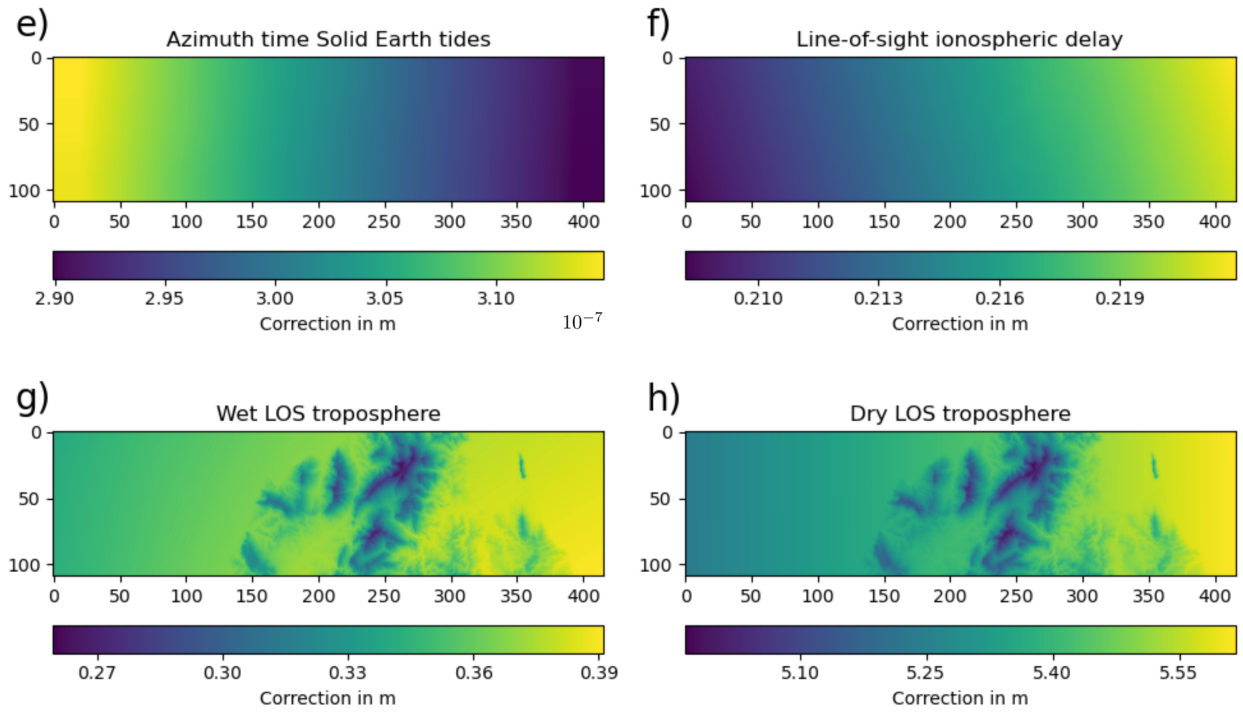


Figure 3. Coregistered SLC timing corrections for the whole burst on 24 March 2020. (**a**) Slant range geometrical Doppler, (**b**) azimuth bistatic delay, (**c**) azimuth FM rate mismatch, (**d**) slant range solid Earth tides, (**e**) azimuth time solid Earth tides, (**f**) line-of-sight ionospheric delay, (**g**) wet LOS troposphere, (**h**) dry LOS troposphere.

Timing corrections effectively mitigate errors in the range and azimuth dimensions, thereby enhancing the alignment of data across repeated observations. This improved alignment is essential for reliable subsequent analyses, as it directly impacts the accuracy of geocoded SLC products.

3.2. Construction and Optimization of the InSAR Network

We constructed an initial redundant network of 780 interferograms over a 5-year period using Delaunay triangulation, with a maximum temporal distance between interferograms of 220 days and a perpendicular baseline of 200 m (Figure 4). This high redundancy allowed for the selection of interferograms that maximize the number of connected components, increasing the number of fully connected pixels from 1241 to 2937.

As shown in Figure 4, the areas with the lowest sum of connected components are located in regions of high port activity, such as the general cargo and container areas and the Juan Carlos I Pier in the Northeast of the AOI. The frequent movement of containers and docked vessels in these areas is likely to cause decorrelation, leading to fewer connected components.

This optimization of the interferogram network significantly improves the reliability of the InSAR analysis, particularly in dynamic environments, as it allows us to preserve the most points in the connected component mask needed for the phase closure correction in Mintpy processing [54].

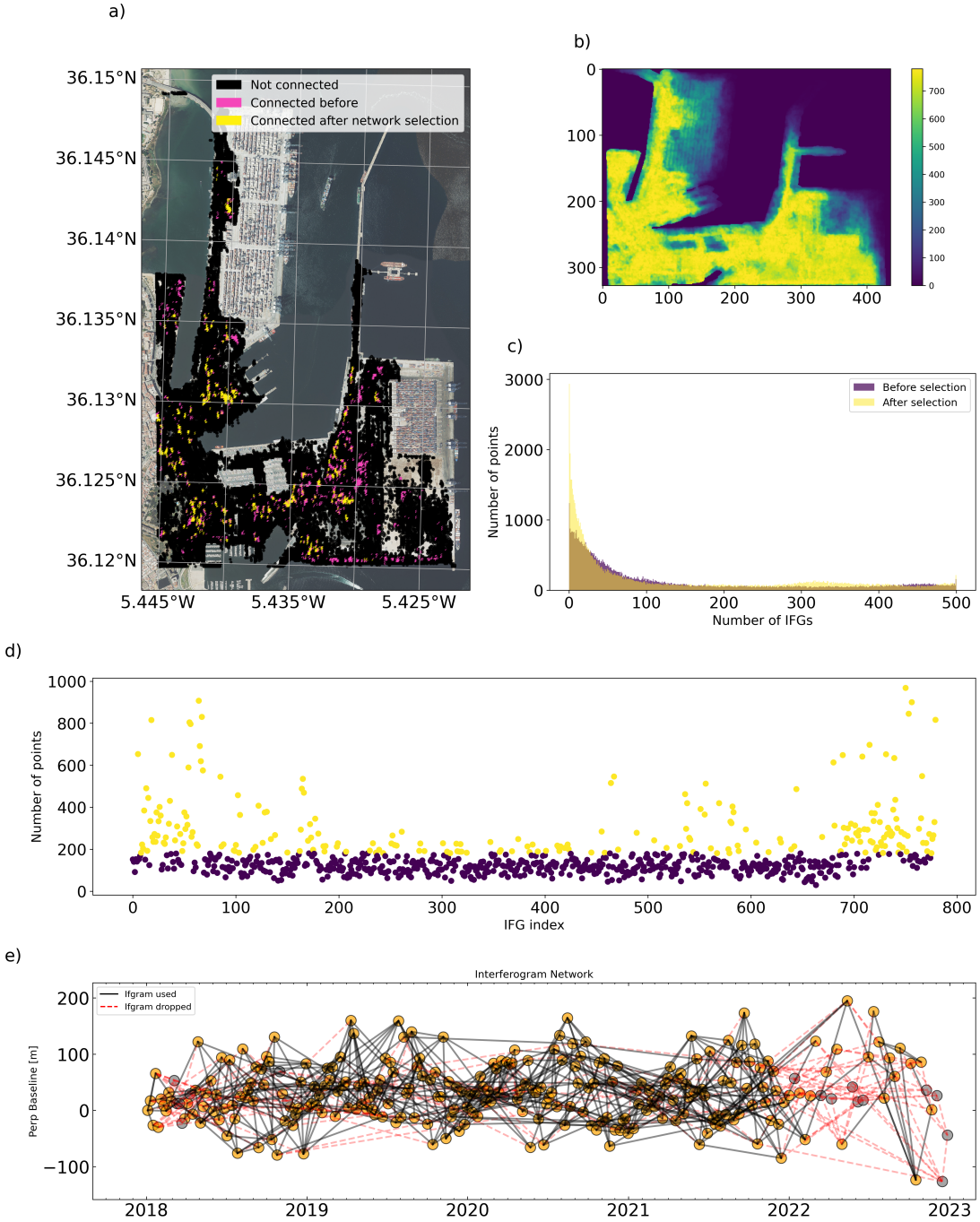


Figure 4. InSAR network selection. (**a**) Mask connected components before (purple) and after (yellow) IFG selection. (**b**) Number of connected components, (**c**) number of IFGs not connected per pixel, (**d**) number of unconnected pixels per IFG, discarted IFGs are shown in yellow, (**e**) IFG network selected.

3.3. Temporal Coherence and Amplitude Dispersion Analysis

Figure 5 illustrates the spatial distribution of temporal coherence and amplitude dispersion across the AOI. Temporal coherence is near 1 for persistent scatterers, indicating high stability over time, while lower coherence is observed for distributed scatterers (DS). The amplitude dispersion is significantly higher in man-made structures, probably because of strong reflections. Out of the total 33,564 pixels, 5683 were classified as PS and 27,881 as DS, although this number is overestimated, as one DS spans many pixels.

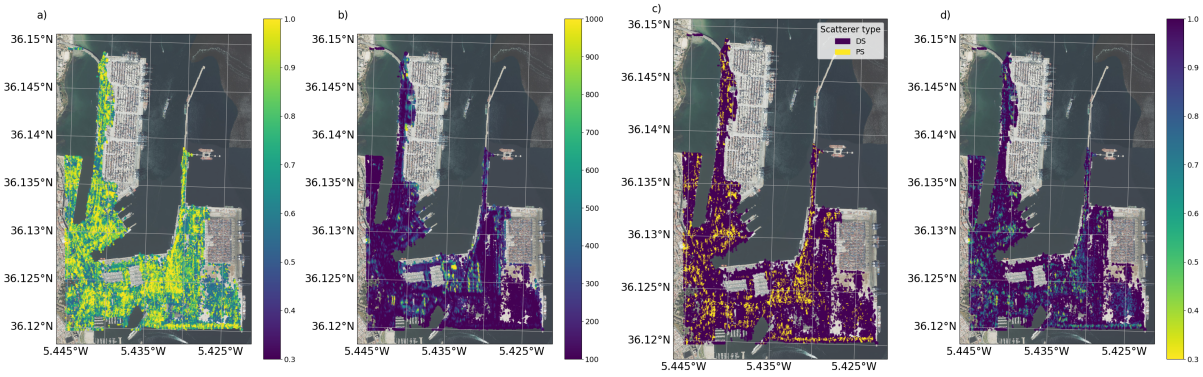


Figure 5. (**a**) Temporal coherence, (**b**) mean amplitude, (**c**) scatterer type, (**d**) amplitude dispersion.

These patterns suggest that persistent scatterers dominate stable areas, as we can see in Figure 5, while DSs are more prevalent in regions with dynamic activity, such as port facilities. This distinction is crucial for interpreting the stability and movement within the AOI, particularly when analyzing long-term displacement patterns.

3.4. Comparison of Velocity Estimations Using Different Processing Workflows

The ground deformation velocities for all points within the Area of Interest (AOI) were calculated using three different processing methodologies: EGMS, ISCE2-MiaplPy, and ISCE3-MiaplPy. As shown in Figure 6 and Table 2, the ISCE3-MiaplPy workflow produced the highest density of measurement points, with a notable increase compared to both EGMS and ISCE2-MiaplPy. Specifically, the density of the points increased by over 300% compared to EGMS and by 130% compared to ISCE2-MiaplPy. This increase can be attributed to the higher resampled resolution of the CSLC products in ISCE3, as well as the application of the eigenvalue criterion [51] in both ISCE2 and ISCE3, which enhances the density of Persistent Scatterers (PS) and includes Distributed Scatterers (DS) that are sparse in the EGMS results.

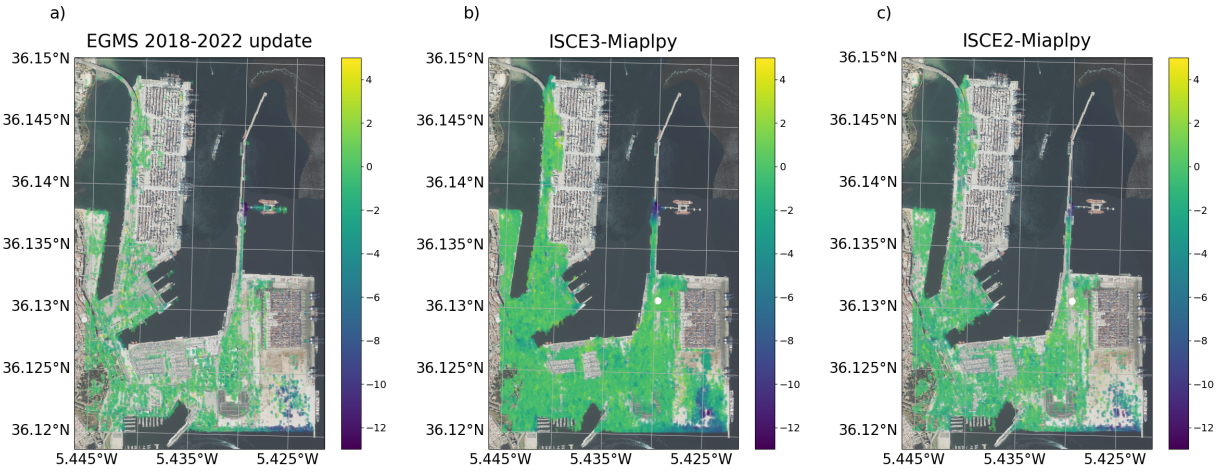


Figure 6. (**a**) EGMS velocity for the Algeciras port. (**b**) Same area processed using CSLCs and phase. (**c**) Same area processed using ISCE2 and geocoding after phase linking. Reference point used for processing highlighted in white for (**b**,**c**).

Table 2. Results summary for different workflows over the AOI.

Workflows	Measurement Points	Mean Vel (mm/year)	STD (mm/year)
ISCE3-MiaPLPy	33,142	−0.63	1.59
ISCE2-MiaPLPy	14,061	−0.67	1.62
EGMS	8041	−0.95	2.12

However, evaluating the point density solely based on percentages may overlook important spatial coverage differences. To provide a more accurate comparison, we assessed the area coverage using a 30 × 30 m grid. The results indicate that ISCE3-MiaplPy achieved a total coverage of 4,633,200 m^2, compared to 4,075,200 m^2 for ISCE2-MiaplPy and 3,237,300 m^2 for EGMS. This represents a 13.7% increase in coverage for ISCE3 relative to ISCE2 and a 43% increase relative to EGMS. These findings suggest that ISCE3 not only improves point density but also extends the spatial coverage, filling gaps that were not covered by other methods, especially EGMS.

A comparison of the velocity histograms (Figure 7) highlights the differences between these workflows. The ISCE3-MiaplPy process consistently provides more detailed and higher-resolution velocity estimates, particularly in areas with dense PS and DS distributions.

In Figures 8 and 9, the time series analysis is focused on two critical areas within Algeciras Port: the EVOS terminal and the development area south of the Isla Verde Exterior breakwater. In the EVOS terminal (Figure 8), the deformation patterns observed using ISCE3 closely align with those detected by the EGMS dataset, with ISCE3 providing slightly better coverage. However, the ISCE3 time series data exhibit more noise, as the mean of the time series exhibits more variance in the ISCE3-MiaplPy process than in EGMS, which may obscure some subtle subsidence patterns. Similarly, in the development area near Isla Verde Exterior (Figure 9), all methods show consistent velocity trends, with ISCE3 offering greater spatial coverage, but at the cost of increased noise.

In general, the comparative analysis of these workflows indicates that, while ISCE3-MiaplPy offers improved coverage to detect deformation patterns across the AOI, it also introduces more noise into the time series. Despite these differences, general deformation trends are consistent across all methods, demonstrating their reliability in monitoring areas with complex activity and infrastructure.

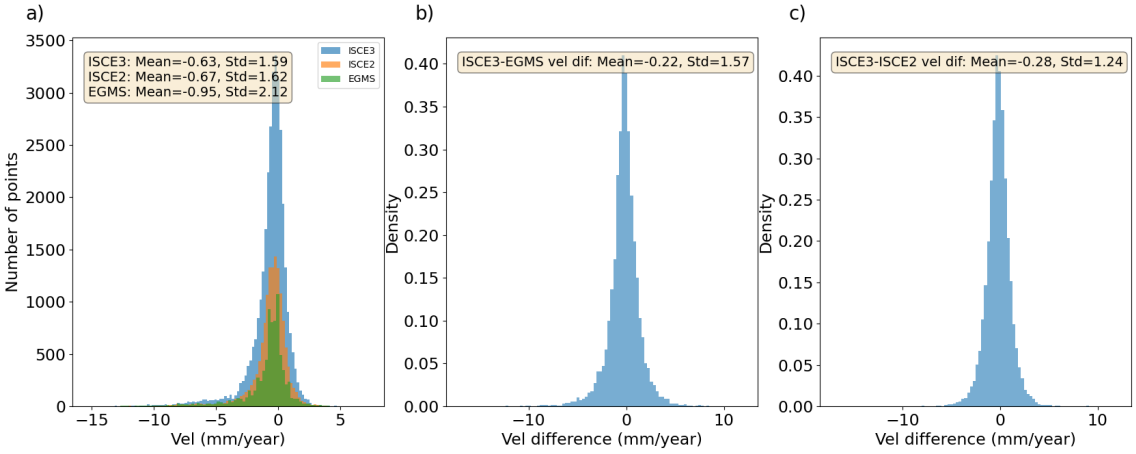


Figure 7. (**a**) Histograms for the velocity in ISCE3-MiaplPy, ISCE2-MiaplPy, and EGMS over the AOI. (**b**) Histogram of velocity differences between ISCE3-EGMS. (**c**) Histogram of velocity differences between ISCE2-ISCE3.

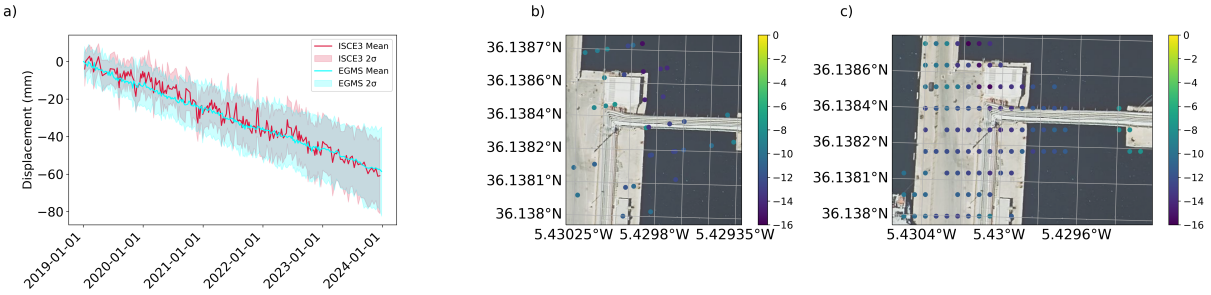


Figure 8. (**a**) Comparison of a group of time series over EVOS Terminal in ISCE3-MiaPLpy and EGMS. (**b**) Measurement points over the area based on EGMS colored by velocity. (**c**) Same for ISCE3-Miaplpy.

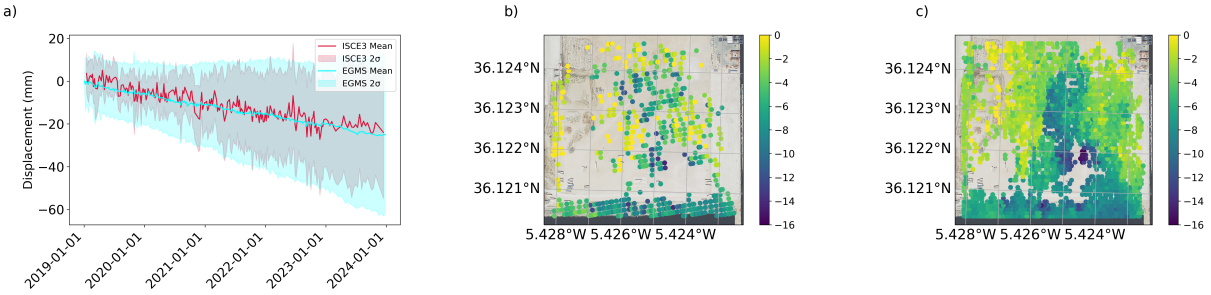


Figure 9. (**a**) Comparison of a group of time series over Isla Verde Exterior in ISCE3-MiaPLpy and EGMS. (**b**) Measurement points over the area based on EGMS colored by velocity. (**c**) Same for ISCE3-Miaplpy.

4. Discussion

In this study, we evaluated the effectiveness of a new open-source InSAR processing workflow that combines Level 2 Coregistered Single Look Complex (L2-CSLC) products with the MiaPLpy software for PSDS processing [46]. This workflow represents the first application of MiaPLpy using L2-CSLC products, providing an opportunity to assess the advantages and limitations of starting InSAR processing from these higher-level products. To validate our approach, we compared the results with those obtained from the European Ground Motion Service (EGMS) and a previous preprocessing methodology using ISCE2.

The use of CSLC products simplifies InSAR workflows by allowing users to start interferometric processing directly, without any initial preprocessing. This streamlining reduces processing time and complexity, making advanced InSAR analysis more accessible to practitioners. Additionally, having fully coregistered intermediate products—such as temporal or spatial coherence maps, connected component masks, and amplitude dispersion images—and the ability to quickly integrate them into any Geographic Information System (GIS) substantially improves the interpretation of the results. As shown in Figure 5, many structural features become apparent just by examining the amplitude dispersion, which can aid in time series analysis. This improvement in data interpretation adds value for both the InSAR expert responsible for generating deformation results and the end user, facilitating more informed decision-making.

Furthermore, advanced timing error corrections included in the CSLC products [28] help mitigate azimuth misregistration errors during geocoding, reducing the need for Enhanced Spectral Diversity (ESD) techniques. This has been demonstrated in Point Target Analysis (PTA), achieving an absolute location error of 0.06 m in range and 0.29 m in azimuth for the Sentinel-1 IW mode [27]. This has also been replicated for CSLC products, with similar results [18,19,55,56]. Our results align with these findings, further validating the utility of CSLC products for infrastructure monitoring.

We evaluated the spatial coverage and density of the measurement points. The ISCE3-MiaPLpy workflow yielded a higher density of coherent measurement points compared

to both EGMS and the ISCE2-MiaPLpy approach. Using a 30 × 30 m grid, we found that ISCE3-MiaPLpy achieved a 13.7% increase in area coverage over ISCE2-MiaPLpy and a 43% increase over EGMS. This increased coverage provides a more detailed understanding of infrastructure stability, which is particularly valuable in dynamic environments such as the Port of Algeciras. However, we also noted that our time series exhibited increased noise levels compared to EGMS, which necessitates careful consideration when interpreting the results. This trade-off between spatial coverage and noise highlights the need for optimizing the processing parameters or incorporating noise reduction techniques in future work.

While this evaluation highlighted several advantages of the new workflow, it also identified areas for future research and improvement. One significant factor is the quality of the Digital Elevation Model (DEM) used during coregistration. Although we used the Copernicus DEM [26] for consistency with EGMS, higher-resolution DEMs from LiDAR or photogrammetric sources could further enhance geolocation accuracy, especially in environments with abrupt elevation changes like ports. Integrating more accurate DEMs over these areas could reduce coregistration errors and, consequently, improve the overall quality of the deformation measurements. This is crucial to correctly attribute observed deformations to specific structural elements within the port infrastructure, which is important for detailed monitoring and risk assessment [57].

Finally, the evaluation indicates the potential for broader application of this workflow. Future studies could explore its effectiveness in monitoring different types of port infrastructure or in combining data from multiple radar bands to capture smaller-scale deformations. Developing a more comprehensive understanding of failure modes linked to satellite data could also facilitate the creation of advanced warning systems based on hypothesis testing, enhancing the capability for real-time monitoring and risk mitigation.

5. Conclusions

This study evaluated an open-source InSAR processing workflow combining Level 2 Coregistered Single Look Complex (L2-CSLC) products with the MiaPLpy software for PSDS processing. Our findings indicate that initiating InSAR processing from L2-CSLC products enhances spatial coverage and increases the density of coherent measurement points compared to previous workflows. Specifically, we observed a 13.7% increase in area coverage over ISCE2-MiaPLpy and a 43% increase over EGMS using a 30 × 30 m grid, offering a more detailed assessment of infrastructure stability in dynamic environments like the Port of Algeciras.

While the increased point density introduces higher noise levels in the time series relative to EGMS, this trade-off highlights the potential for further optimization of processing parameters or incorporation of noise reduction techniques. The advanced timing error corrections in CSLC products contribute to improved geolocation accuracy, validating the utility of these products for infrastructure monitoring.

Overall, this evaluation demonstrates that the ISCE3-MiaPLpy workflow is a valuable tool for InSAR analysis in port environments, providing enhanced data quality and interpretation capabilities. The streamlined, open-source nature of the workflow makes advanced InSAR processing more accessible, which can significantly benefit infrastructure monitoring and risk assessment efforts. Adapting this workflow to other types of critical infrastructure could further extend its impact, supporting broader applications in the field of geospatial analysis and remote sensing.

Author Contributions: Conceptualization, J.S.-F., A.F.-L. and R.M.S.; methodology, J.S.-F.; software, J.S.-F. and Á.H.C.; validation, J.S.-F., A.F.-L. and R.M.S.; investigation, J.S.-F.; writing—original draft preparation, J.S.-F.; writing—review and editing, A.F.-L., Á.H.C. and R.M.S. All authors have read and agreed to the published version of the manuscript.

Funding: This research received public funds through the industrial doctorates program DIN2020-011531, provided by the Spanish Ministry of Science and Innovation and the State Research Agency (MCIN/AEI/10.13039/501100011033) and by the European Union NextGenerationEU/PRTR initiative.

Data Availability Statement: The raw data supporting the conclusions of this article will be made available by the authors upon request.

Acknowledgments: The authors would like to acknowledge the support of the Ports 4.0 Ports of Spain Tradetech Fund and the Autoridad Portuaria de Bahía de Algeciras. The authors extend special thanks to the OPERA Team at JPL and the Rosenstiel School of Marine and Atmospheric Science, University of Miami, for developing the open-source software suite that made the integrated workflow possible. The first author is supported by the Industrial Doctorates grant (DIN2020-011531).

Conflicts of Interest: Authors Jaime Sánchez-Fernández, Alfredo Fernández-Landa and Álvaro Hernández Cabezudo were employed by the company Detektia Earth Surface Monitoring S.L. The remaining authors declare that the research was conducted in the absence of any commercial or financial relationships that could be construed as a potential conflict of interest.

Abbreviations

The following abbreviations are used in this manuscript:

InSAR	Interferometric Synthetic Aperture Radar
PSDS	Persistent Scatterer and Distributed Scatterer
L2-CSLC	Level 2 Coregistered Single Look Complex
CPL	Combined eigenvalue maximum likelihood Phase Linking
COMPASS	Coregistered Multi-temporal Sar SLC
EGMS	European Ground Motion Service
ISCE	InSAR Scientific Computing Environment
SLC	Single Look Complex
DEM	Digital Elevation Model
PNOA	National Aerial Orthophotography Plan
SBAS	Small Baseline Subset
SHP	Statistical Homogeneous Pixels
CCM	Complex Covariance Matrix
MLE	Maximum Likelihood Estimation
PTA	Point Target Analysis
ALE	Absolute Location Error
CRS	Coordinate Reference System
ETAD	Enhanced Timing Annotation Dataset
ERA5	ECMWF Reanalysis, 5th Generation
MiaplPy	Miami InSAR Time-Series Software in Python
MintPy	Miami Insar Timeseries software in Python
Raider	Ray-tracing Atmospheric Delay Estimation for InSAR
OPERA	Open Platform for Earth Observation-Based Radar Applications
PSI	Persistent Scatterer Interferometry
PL	Phase Linking
IFG	Interferogram
LOS	Line of Sight

References

1. Pavlic, B.; Cepak, F.; Sucic, B.; Peckaj, M.; Kandus, B. Sustainable port infrastructure, practical implementation of the green port concept. *Therm. Sci.* **2014**, *18*, 935–948. [CrossRef]
2. Zhang, Y.; Kim, C.W.; Tee, K.F.; Lam, J.S.L. Optimal sustainable life cycle maintenance strategies for port infrastructures. *J. Clean. Prod.* **2017**, *142*, 1693–1709. [CrossRef]
3. Campos, A.; Molina-Sanchez, R.; Castillo, C. Damage in Rubble Mound Breakwaters. Part II: Review of the Definition, Parameterization, and Measurement of Damage. *J. Mar. Sci. Eng.* **2020**, *8*, 306. [CrossRef]
4. Castillo, C.; Castillo, E.; Fernández-Canteli, A.; Molina, R.; Gómez, R. Stochastic Model for Damage Accumulation in Rubble-Mound Breakwaters Based on Compatibility Conditions and the Central Limit Theorem. *J. Waterw. Port Coastal Ocean. Eng.* **2012**, *138*, 451–463. [CrossRef]

5. de Almeida, E.; van Gent, M.R.A.; Hofland, B. Damage Characterization of Rock Slopes. *J. Mar. Sci. Eng.* **2019**, *7*, 10. [CrossRef]
6. Tomás, R.; Romero, R.; Mulas, J.; Marturià, J.J.; Mallorquí, J.J.; Lopez-Sanchez, J.M.; Herrera, G.; Gutiérrez, F.; González, P.J.; Fernández, J.; et al. Radar interferometry techniques for the study of ground subsidence phenomena: A review of practical issues through cases in Spain. *Environ. Earth Sci.* **2014**, *71*, 163–181. [CrossRef]
7. Seidel, M.; Marzahn, P.; Ludwig, R. Monitoring of Sea Dike Structures by the Means of Combined StaMPS Multi-temporal InSAR Approach. *Procedia Comput. Sci.* **2016**, *100*, 1147–1154. [CrossRef]
8. Özer, I.E.; Rikkert, S.J.; van Leijen, F.J.; Jonkman, S.N.; Hanssen, R.F. Sub-seasonal Levee Deformation Observed Using Satellite Radar Interferometry to Enhance Flood Protection. *Sci. Rep.* **2019**, *9*, 2646. [CrossRef]
9. Mirzaee, S.; Amelung, F.; Fattahi, H. Non-linear phase linking using joined distributed and persistent scatterers. *Comput. Geosci.* **2023**, *171*, 105291. [CrossRef]
10. Fattahi, H.; Agram, P.; Simons, M. A Network-Based Enhanced Spectral Diversity Approach for TOPS Time-Series Analysis. *IEEE Trans. Geosci. Remote Sens.* **2017**, *55*, 777–786. [CrossRef]
11. Wu, Z.; Ellingsen, P.G.; Jia, H.; ÅDland, R.O. Tracking Volume Change of the Bulk Commodities with Interferometric SAR. In Proceedings of the IGARSS 2023—2023 IEEE International Geoscience and Remote Sensing Symposium, Pasadena, CA, USA, 16–21 July 2023; pp. 8242–8245. [CrossRef]
12. Tirmizi, O.; Khan, S.D. Factors of Subsidence in Katy, Texas, USA. *Remote Sens.* **2023**, *15*, 4424. [CrossRef]
13. Zhang, G.; Yu, Z.; Zhang, Z.; Jiang, W.; Zhang, Y. Deformation monitoring of Shuangwangcheng Reservoir based on time-series InSAR method. In Proceedings of the Fifth International Conference on Geoscience and Remote Sensing Mapping (ICGRSM 2023), Lianyungang, China, 13–15 October 2023; p. 103. [CrossRef]
14. Fattahi, H.; Bekaert, D.P.; Brancato, V.; Yunjun, Z.; Lu, Z.; Bato, M.G.; Kim, J.W.; Jeong, S.; Liang, K.; Sangha, S. OPERA Coregistered Single Look Complex products from Sentinel-1 data. In Proceedings of the AGU Fall Meeting, Chicago, IL, USA, 12–16 December 2022; Volume 2022, p. G45A–03.
15. NASA; JPL; OPERA. *OPERA OPERA Level-2 Coregistered Single-Look Complex Static Layers from Sentinel-1*; NASA Alaska Satellite Facility Distributed Active Archive Center: Fairbanks, AK, USA, 2023. [CrossRef]
16. NASA; JPL; OPERA. *OPERA Level-2 Coregistered Single-Look Complex from Sentinel-1*; NASA Alaska Satellite Facility Distributed Active Archive Center: Fairbanks, AK, USA, 2023. [CrossRef]
17. Rosen, P.A.; Gurrola, E.M.; Agram, P.; Cohen, J.; Lavalle, M.; Riel, B.V.; Fattahi, H.; Aivazis, M.A.; Simons, M.; Buckley, S.M. The InSAR Scientific Computing Environment 3.0: A Flexible Framework for NISAR Operational and User-Led Science Processing. In Proceedings of the IGARSS 2018—2018 IEEE International Geoscience and Remote Sensing Symposium, Valencia, Spain, 22–27 July 2018; pp. 4897–4900. [CrossRef]
18. Yunjun, Z.; Fattahi, H.; Brancato, V.; Liu, Y.K.; Simons, M. Azimuth Geolocation of Sentinel-1 and Its Implications for Stack Coregistration and Intra-Burst Phase Discontinuity. In Proceedings of the AGU Fall Meeting, Chicago, IL, USA, 12–16 December 2022.
19. Yunjun, Z.; Fattahi, H.; Pi, X.; Rosen, P.; Simons, M.; Agram, P.; Aoki, Y. Range Geolocation Accuracy of C-/L-Band SAR and its Implications for Operational Stack Coregistration. *IEEE Trans. Geosci. Remote Sens.* **2022**, *60*, 1–19. [CrossRef]
20. Ansorena, I.L. Analysing the maritime network of the port of Algeciras Bay. *World Rev. Intermodal Transp. Res.* **2020**, *9*, 245–263. [CrossRef]
21. Alfonso, C. "Gateway" City and Nexus Between Two Continents: The Port City of Algeciras. In *Port Cities as Areas of Transition*; Transcript Verlag: Bielefeld, Germany, 2008. [CrossRef]
22. Acosta, M.; Coronado, D.; Mar Cerban, M. Port competitiveness in container traffic from an internal point of view: The experience of the Port of Algeciras Bay. *Marit. Policy Manag.* **2007**, *34*, 501–520. [CrossRef]
23. Gil-Ropero, A.; Cerban, M.; Turias, I.J. Analysis of the Global and Technical Efficiencies of Major Spanish Container Ports. *Int. J. Transp. Econ./Riv. Internazionale Econ. Dei Trasp.* **2015**, *42*, 377–407.
24. Costantini, M.; Minati, F.; Trillo, F.; Ferretti, A.; Novali, F.; Passera, E.; Dehls, J.; Larsen, Y.; Marinkovic, P.; Eineder, M.; et al. European Ground Motion Service (EGMS). In Proceedings of the 2021 IEEE International Geoscience and Remote Sensing Symposium IGARSS, Brussels, Belgium, 11–16 July 2021; pp. 3293–3296. [CrossRef]
25. European Environment Agency. European Ground Motion Service: Basic 2018–2022 (Vector), Europe, Yearly, Oct. 2023. 2023. Available online: https://sdi.eea.europa.eu/catalogue/srv/api/records/1b2eb0d6-8c3a-4de2-b99d-10a30079f3cc (accessed on 22 October 2024) [CrossRef]
26. European Space Agency; Airbus. *Copernicus DEM*; European Space Agency: Paris, France, 2022. [CrossRef]
27. Gisinger, C.; Schubert, A.; Breit, H.; Garthwaite, M.; Balss, U.; Willberg, M.; Small, D.; Eineder, M.; Miranda, N. In-Depth Verification of Sentinel-1 and TerraSAR-X Geolocation Accuracy Using the Australian Corner Reflector Array. *IEEE Trans. Geosci. Remote Sens.* **2021**, *59*, 1154–1181. [CrossRef]
28. Gisinger, C.; Libert, L.; Marinkovic, P.; Krieger, L.; Larsen, Y.; Valentino, A.; Breit, H.; Balss, U.; Suchandt, S.; Nagler, T.; et al. The Extended Timing Annotation Dataset for Sentinel-1—Product Description and First Evaluation Results. *IEEE Trans. Geosci. Remote Sens.* **2022**, *60*, 1–22. [CrossRef]

29. Maurer, J.; Bekaert, D.; Sangha, S.; Hamlington, B.; Marshak, C.; Lei, Y.; Kumar, P.; Fattahi, H. RAiDER: Raytracing Atmospheric Delay Estimation for RADAR. In Proceedings of the AGU Fall Meeting, New Orleans, LA, USA, 13–17 December 2021; Volume 2021, p. G44A–07.
30. Hersbach, H.; Bell, B.; Berrisford, P.; Hirahara, S.; Horányi, A.; Muñoz-Sabater, J.; Nicolas, J.; Peubey, C.; Radu, R.; Schepers, D.; et al. The ERA5 global reanalysis. *Q. J. R. Meteorol. Soc.* **2020**, *146*, 1999–2049. [CrossRef]
31. Noll, C.E. The crustal dynamics data information system: A resource to support scientific analysis using space geodesy. *Adv. Space Res.* **2010**, *45*, 1421–1440. [CrossRef]
32. Ferretti, A.; Fumagalli, A.; Novali, F.; Prati, C.; Rocca, F.; Rucci, A. A New Algorithm for Processing Interferometric Data-Stacks: SqueeSAR. *IEEE Trans. Geosci. Remote Sens.* **2011**, *49*, 3460–3470. [CrossRef]
33. Ferretti, A. End-to-End Implementation and Operation of the European Ground Motion Service (EGMS). 2023. Available online: https://land.copernicus.eu/en/technical-library/egms-algorithm-theoretical-basis-document/@@download/file (accessed on 22 October 2024).
34. Agram, P.S.; Warren, M.S.; Calef, M.T.; Arko, S.A. An Efficient Global Scale Sentinel-1 Radar Backscatter and Interferometric Processing System. *Remote Sens.* **2022**, *14*, 3524. [CrossRef]
35. Zebker, H.A.; Goldstein, R.M. Topographic mapping from interferometric synthetic aperture radar observations. *J. Geophys. Res.* **1986**, *91*, 4993. [CrossRef]
36. OPERA CSLC-S1 Static Layers Product Description, 2023. Available online: https://asf.alaska.edu/wp-content/uploads/2023/11/OPERA-CSLC-S1-ProductSpec-v1.0.0-D-108278-Initial-2023-09-11-URS321269.pdf (accessed on 22 October 2024).
37. Prats-Iraola, P.; Scheiber, R.; Marotti, L.; Wollstadt, S.; Reigber, A. TOPS Interferometry with TerraSAR-X. *IEEE Trans. Geosci. Remote Sens.* **2012**, *50*, 3179–3188. [CrossRef]
38. Bara, M.; Moreira, A. Interferometric SAR Signal Analysis in the Presence of Squint. *IEEE Trans. Geosci. Remote Sens.* **2000**, *38*, 2164–2178. [CrossRef]
39. Rodriguez-Cassola, M.; Prats-Iraola, P.; De Zan, F.; Scheiber, R.; Reigber, A.; Geudtner, D.; Moreira, A. Doppler-Related Distortions in TOPS SAR Images. *IEEE Trans. Geosci. Remote Sens.* **2015**, *53*, 25–35. [CrossRef]
40. De Zan, F.; Prats-Iraola, P.; Scheiber, R.; Rucci, A. Interferometry with TOPS: Coregistration and azimuth shifts. In Proceedings of the EUSAR 2014, 10th European Conference on Synthetic Aperture Radar, Berlin, Germany, 3–5 June 2014.
41. Milbert, D. Solid: Solid Earth Tide, 2018. Available online: http://geodesyworld.github.io/SOFTS/solid.htm (accessed on 22 October 2024).
42. De Zan, F.; Lopez-Dekker, P. SAR Image Stacking for the Exploitation of Long-Term Coherent Targets. *IEEE Geosci. Remote Sens. Lett.* **2011**, *8*, 502–506. [CrossRef]
43. Guarnieri, A.M.; Tebaldini, S. On the Exploitation of Target Statistics for SAR Interferometry Applications. *IEEE Trans. Geosci. Remote Sens.* **2008**, *46*, 3436–3443. [CrossRef]
44. Guarnieri, A.; Tebaldini, S. Hybrid CramÉr–Rao Bounds for Crustal Displacement Field Estimators in SAR Interferometry. *IEEE Signal Process. Lett.* **2007**, *14*, 1012–1015. [CrossRef]
45. Ansari, H.; Adam, N.; Brcic, R. Amplitude time series analysis in detection of persistent and temporal coherent scatterers. In Proceedings of the 2014 IEEE Geoscience and Remote Sensing Symposium, Quebec City, QC, Canada, 13–18 July 2014; pp. 2213–2216. [CrossRef]
46. Ansari, H. Synthetic Aperture Radar Interferometry. Ph.D. Thesis, Technische Universität München, Munich, Germany, 2018.
47. Lanari, R.; Mora, O.; Manunta, M.; Mallorqui, J.; Berardino, P.; Sansosti, E. A small-baseline approach for investigating deformations on full-resolution differential SAR interferograms. *IEEE Trans. Geosci. Remote Sens.* **2004**, *42*, 1377–1386. [CrossRef]
48. Ansari, H.; De Zan, F.; Bamler, R. Efficient Phase Estimation for Interferogram Stacks. *IEEE Trans. Geosci. Remote Sens.* **2018**, *56*, 4109–4125. [CrossRef]
49. Ansari, H.; De Zan, F.; Bamler, R. Sequential Estimator: Toward Efficient InSAR Time Series Analysis. *IEEE Trans. Geosci. Remote Sens.* **2017**, *55*, 5637–5652. [CrossRef]
50. Ferretti, A.; Prati, C.; Rocca, F. Permanent scatterers in SAR interferometry. *IEEE Trans. Geosci. Remote Sens.* **2001**, *39*, 8–20. [CrossRef]
51. Navneet, S.; Kim, J.W.; Lu, Z. A New InSAR Persistent Scatterer Selection Technique Using Top Eigenvalue of Coherence Matrix. *IEEE Trans. Geosci. Remote Sens.* **2018**, *56*, 1969–1978. [CrossRef]
52. Chen, C.W.; Zebker, H.A. Network approaches to two-dimensional phase unwrapping: Intractability and two new algorithms. *J. Opt. Soc. Am. A* **2000**, *17*, 401. [CrossRef]
53. Hooper, A.; Zebker, H.; Segall, P.; Kampes, B. A new method for measuring deformation on volcanoes and other natural terrains using InSAR persistent scatterers. *Geophys. Res. Lett.* **2004**, *31*, 2004GL021737. [CrossRef]
54. Yunjun, Z.; Fattahi, H.; Amelung, F. Small baseline InSAR time series analysis: Unwrapping error correction and noise reduction. *Comput. Geosci.* **2019**, *133*, 104331. [CrossRef]
55. Observational Products for End-Users from Remote Sensing Analysis (OPERA)—Product Validation Plan. V1.5. Available online: https://d2pn8kiwq2w21t.cloudfront.net/documents/OPERA_Validation_Plan.pdf (accessed on 22 October 2024).

56. Bekaert, D. OPERA Analysis-Ready SAR and Optical Products for Mapping Water Extent, Disturbance, and Displacement at Continental to Near-Global Scales, 2023. Available online: https://fringe2023.esa.int/iframe-agenda/files/presentation-262.pdf (accessed on 22 October 2024).
57. Dheenathayalan, P. Optimizing the Exploitation of Persistent Scatterers in Satellite Radar Interferometry. Ph.D. Thesis, Delft University of Technology, Delft, The Netherlands, 2019. [CrossRef]

Disclaimer/Publisher's Note: The statements, opinions and data contained in all publications are solely those of the individual author(s) and contributor(s) and not of MDPI and/or the editor(s). MDPI and/or the editor(s) disclaim responsibility for any injury to people or property resulting from any ideas, methods, instructions or products referred to in the content.